



Bifunctional catalytic material: An ultrastable and high-performance surface defect CeO₂ nanosheets for formaldehyde thermal oxidation and photocatalytic oxidation

Yongchao Huang^a, Bei Long^b, Minni Tang^a, Zebao Rui^a, Muhammad-Sadeeq Balogun^b, Yexiang Tong^{b,*}, Hongbing Ji^{a,*}

^a The Key Lab of Low-carbon Chem & Energy Conservation of Guangdong Province, School of Chemistry and Chemical Engineering, Sun Yat-Sen University, 135 Xingang West Road, Guangzhou 510275, PR China

^b MOE of the Key Laboratory of Bioinorganic and Synthetic Chemistry, KLGHEI of Environment and Energy Chemistry, The Key Lab of Low-carbon Chem & Energy Conservation of Guangdong Province, Sun Yat-Sen University, 135 Xingang West Road, Guangzhou 510275, PR China



ARTICLE INFO

Article history:

Received 19 June 2015

Received in revised form 25 August 2015

Accepted 29 August 2015

Available online 2 September 2015

Keywords:

CeO₂ nanosheets

Surface defect

Formaldehyde

Thermal catalytic oxidation

Photocatalytic oxidation

ABSTRACT

Eu-doped CeO₂ nanosheets were obtained on Ti substrate by facile anodic electrodeposition and annealing in N₂ atmosphere. The composition of the Eu cations doped into the CeO₂ nanosheets can be easily tuned by adjusting the ratio of Eu to Ce, which promoted the formation of surface defects. Compared to pristine CeO₂ nanosheets, the as-prepared 4% Eu/CeO₂ nanosheets exhibited a much lower complete temperature (120 °C) of thermal oxidation for HCHO and a much longer stability as long as 100 h. Significantly, the Eu-doped CeO₂ nanosheets also show a much improved photocatalytic performance for removing HCHO under the visible light irradiation. The excellent performance of 4% Eu/CeO₂ nanosheets could be attributed to the abundance of surface defects, high specific surface area and large pore volume, high redox ability, narrowed band gap and enhanced optical absorption, and excellent response in the visible region of solar spectrum. Therefore, this work provides a facile and cost-effective strategy for the design and fabrication of multifunctional catalyst toward HCHO removal.

© 2015 Elsevier B.V. All rights reserved.

1. Introduction

Formaldehyde (HCHO), a naturally occurring and toxic organic compound, is recognized as one of the major contributor to air pollution. It is not only hazardous to human health but also harmful to the environment. Controlling the emission of HCHO has become an important issue in the research world. Recently, great efforts have been developed to eliminate the HCHO pollution indoor, such as adsorption of porous materials [1,2], plasma technology [3], photocatalytic oxidation [4,5], and thermal catalytic oxidation [6]. As energy efficient and environmental benign approaches, thermal catalytic oxidation and photocatalytic oxidation under ambient condition are receiving great attention due to the fact that their end products i.e., CO₂ and H₂O are harmless to human health. However, the development of an efficient, stable, and multifunctional catalyst that could oxidize HCHO under mild condition is the main bottle-

neck of these two methods. To the best of our knowledge, there are few reports on catalysts that can serve as bifunctional material for the emission of HCHO through thermal catalytic and photocatalytic oxidation. Therefore, it still remains a great challenge to synthesize multifunctional catalyst for HCHO oxidation.

Ceria (CeO₂) is a multifunctional rare earth oxide with excellent physical and chemical properties, which has been extensively explored for several advanced applications in the fields of heterogeneous catalysis, electrochemistry, photochemistry, and material science [7–11]. It has also attracted much attention due to its ability to act as primary oxygen storage material. Moreover, CeO₂ is a highly stable fluorite structure with presence of Ce⁴⁺ and Ce³⁺, which gives rise to oxygen vacancies in their structure. Such reducibility in CeO₂ has been found to be enhanced by the proximity of metallic atoms in the form of dopants [12]. Due to the fact that the catalytic activity of CeO₂ originates from the surface oxygen, the active oxygen content at the CeO₂ surface must be increased to improve catalytic activities [13,14]. As a result, it is necessary to study the impact of surface oxygen defect in the structure of CeO₂.

Oxygen vacancy is a fundamental and intrinsic defect in metal oxide semiconductor and has a substantial effect on their elec-

* Corresponding author.

E-mail addresses: chedhx@mail.sysu.edu.cn (Y. Tong), jihb@mail.sysu.edu.cn (H. Ji).

tronic and physicochemical properties [15,16]. Additionally, recent progress in developing oxygen vacancies has strengthened the interest in engineering oxide-based photocatalysts by creating a large number of oxygen vacancies in the surface region because the electronic structures of materials can be significantly changed even with very low vacancy. Many experimental results revealed that the oxygen vacancy played an important role in the defect mediated energy transfer between a photocatalyst and the reactant molecule. Interestingly, the oxygen vacancies are easily formed in the CeO₂, and even in small amounts, seem to favor reaction because they provide sites for oxygen activation to form superoxide species. This was also confirmed theoretically by Sayle et al. [17]. There are several methods of inducing oxygen vacancy in metal oxides. Homogeneous doping of appropriate heteroatoms is one of an efficient way to introduce vacancy into the catalysts. Impressively, CeO₂ has also exhibit much improved properties under doping. For example, doping lower valence ions such as Pr³⁺ and Tb³⁺ in CeO₂ have influenced the energetic properties by lowering the activation energy for oxygen migration [18], while smaller ions enhance the oxygen storage capacity (OSC), preserving oxygen defects and retarding OSC degradation at high temperature [19,20]. Recently, rare-earth ion doped CeO₂ nanostructures has received increasing interest because rare-earth ion doping is a widely applied technological process in materials science that involves incorporating atoms or ions of appropriate elements into host lattices to yield hybrid materials with desirable properties and functions [21]. For instance, Gd³⁺-doped CeO₂ nanomaterials have shown enhanced optical and catalytic properties and potential applications in compact solid oxide fuel cells for their enhancement in oxygen exchange processes [22]. Eu-doped CeO₂ nanostructures have attracted much attention because of their physical and chemical properties due to the increase of oxygen vacancies in the CeO₂ [23,24], likewise, the reactivity of CO oxidation was remarkably enhanced by the doping of Pr in the CeO₂. Given the effects that low valence states have on properties and defect reaction energies, there could be considerable scientific and technological value for intruding ions having lower valence into the CeO₂ lattice and for identifying their role in defect chemistry. Moreover, rare-earth ion doped CeO₂ as a bi-functional catalyst for thermal catalytic oxidation and photocatalysis is very immature.

In this work, Eu³⁺ was doped into CeO₂ nanosheets to boost the surface defect in the CeO₂ structure by simple electrochemical deposition. The composition of the Eu-doped CeO₂ nanosheets can be easily tuned by adjusting the ratio of Eu to Ce. The doping of Eu cations promoted the formation of oxygen vacancy, enhanced the redox ability, and allowed easier surface reaction, which is in favour of catalytic reaction and had excellent response in the visible region of solar spectrum. More importantly, the as-prepared Eu-doped CeO₂ nanosheets are shown to be a promising catalytic material for the oxidation of HCHO at low temperature and removal of HCHO under the visible light irradiation.

2. Experimental

2.1. Preparation of CeO₂ nanosheets

The CeO₂ nanosheets and Eu-doped CeO₂ nanosheets were prepared by depositing onto the substrate by anodic electrodeposition. The electrodeposition was conducted in a solution (15 mL) containing cerous nitrate (0.01 M), europium nitrate (0.001 M) and ammonium nitrate (0.1 M) at -0.2 mA for 60 min at 70 °C, in which Eu contents were 1, 2, 4 and 8 at%, respectively. The resultant produce was washed with distilled water to remove impurities and then dried overnight. The precursor nanorods were annealed in N₂ at 550 °C for 1 h. The composition of the Eu-doped CeO₂ nanosheets

can be easily tuned by adjusting the ratio of Eu to Ce. The final products with different Eu content named 1% Eu/CeO₂, 2% Eu/CeO₂, 4% Eu/CeO₂, 8% Eu/CeO₂ were obtained.

2.2. Characterization

X-ray diffraction (XRD) measurements were performed using a Broker's D8 ADVANCE powder X-ray diffractometer with Cu K radiation ($\lambda = 1.5418 \text{ \AA}$). Transmission electron microscopy (TEM) images were obtained with a JEM2010-HR electron microscope. Samples morphology was investigated by a field emission scanning electron microscope. X-ray photoelectron spectroscopy (XPS) measurements were performed on a ESCALab250 XPS system with Al K α source and a charge neutralizer, and all the binding energies were referenced to the C 1s peak at 284.8 eV of the surface adventurous carbon. Temperature-programmed reduction (TPR) analysis was conducted on a T-5080 Autochem analyzer. About 50 mg of the sample was loaded in a tube-shaped quartz cell above a small amount of quartz wool. The TPR profile of sample was recorded between 35 °C and 800 °C at a heating rate of 10 °C·min⁻¹ in 10% hydrogen in N₂ with a flow rate of 50 mL·min⁻¹. Hydrogen uptake was monitored by TCD detector. Specific surface areas (S_{BET}) of the catalysts were calculated from a multipoint Braunauer-Emmett-Teller (BET) analysis of the nitrogen adsorption and desorption isotherms at 77K recorded on an Autosorb-1 apparatus. The contact angles of HCHO drops deposited on the surface of film were measured at 25 °C using a contact angle meter (SL150, Kino Industrial Co., Ltd., USA).

2.3. Thermal catalytic reaction tests

The HCHO oxidation was performed in a fixed-bed reactor with 0.2 g catalyst. HCHO gas was generated and injected in an incubator (filled with a solution of 37% HCHO) kept at 0 °C, using a purified air flow (N₂/O₂ = 4100 mL·min⁻¹). Gas hourly space velocity (GHSV) of 30,000 mL·h⁻¹·g⁻¹ was applied. Phenol spectrophotometric method was carried out to analyze the HCHO concentration. The gas stream was injected in 5 mL C₆H₄SN(CH₃)C:NNH₂·HCl solution to absorb HCHO for 30 s and 0.4 mL (1 wt.%) ammonium ferric sulfate (NH₄Fe(SO₄)₂ ·12H₂O) solution was added. The mixed solution was shaken and stayed for 15 min in the dark, than the HCHO concentration was detected by the spectrophotometer with the light absorbance at 630 nm. The conversion of HCHO was calculated based on its concentration change.

2.4. Photocatalytic reaction tests

The photocatalytic activity of the as-synthesized samples was evaluated by removing HCHO at 500 ppm in a closed reactor. The reactor had a capacity of 4.5 L (30 cm × 15 cm × 10 cm), made of polymeric glass and covered with Saint-Glass. A commercial tungsten halogen lamp (100 W) was vertically placed 20 cm above the reactor and the photo-catalytic reaction under the condition of constant temperature at 25 °C. A UV cut off filter (420 nm) was applied to remove UV light for tests of visible light photocatalytic activity. The as-prepared sample (0.1 g) was dispersed in the reactor. When the adsorption-desorption equilibrium was achieved, the lamp was turned on. The products of the reaction were analyzed online by an Agilent 7890A gas chromatograph with a TCD detector and a Porapak-Q column. No other carbon-containing compounds except CO₂ in the products were detected for all the tested catalysts. The HCHO conversion was calculated from the CO₂ content as follows:

$$\text{HCHO conversion}(\%) = [\text{CO}_2]_{\text{out}} / [\text{HCHO}]_{\text{in}} \times 100$$

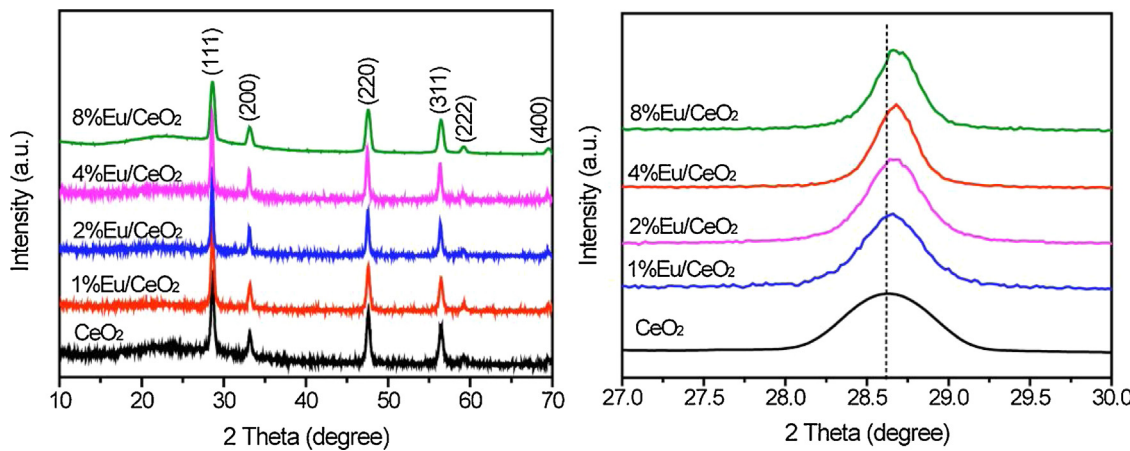


Fig. 1. XRD pattern of CeO_2 nanosheets, 1% Eu/ CeO_2 nanosheets, 2% Eu/ CeO_2 nanosheets, 4% Eu/ CeO_2 nanosheets, and 8% Eu/ CeO_2 nanosheets.

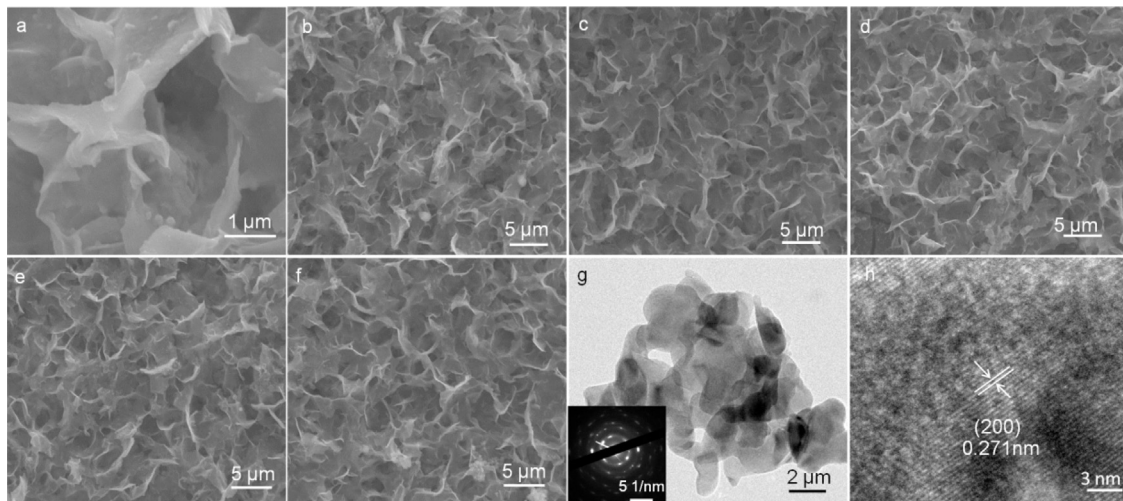


Fig. 2. SEM of the (a) 4% Eu/ CeO_2 nanosheets, (b) CeO_2 nanosheets, (c) 1% Eu/ CeO_2 nanosheets, (d) 2% Eu/ CeO_2 nanosheets, (e) 4% Eu/ CeO_2 nanosheets, and (f) 8% Eu/ CeO_2 nanosheets. (g) TEM image and SAED pattern of the 4% Eu/ CeO_2 nanosheets. (h) HRTEM image of 4% Eu/ CeO_2 nanosheets.

$[\text{CO}_2]_{\text{out}}$ and $[\text{HCHO}]_{\text{in}}$ in the formula are the CO_2 concentration in the products and the HCHO concentration in the reactor, respectively. CO_2 selectivity was defined as the ratio of HCHO oxidized into CO_2 to the total removed HCHO.

3. Result and discussion

3.1. ICP analysis

The composition of the Eu-doped CeO_2 nanosheets were identified by inductively coupled plasma (ICP) and the corresponding content of Eu were displayed in Table 1. The results are generally consistent with the expected ratio between Ce and Eu based on the precursor electrolyte. The final products with different Eu content named 1% Eu/ CeO_2 , 2% Eu/ CeO_2 , 4% Eu/ CeO_2 , 8% Eu/ CeO_2 were obtained. The composition of the Eu-doped CeO_2 nanosheets can be easily tuned by adjusting the ratio of Eu to Ce.

3.2. XRD analysis

The structural information of the samples was revealed by X-ray diffraction (XRD) pattern. Fig. 1 shows the XRD pattern of the CeO_2 , 1% Eu/ CeO_2 , 2% Eu/ CeO_2 , 4% Eu/ CeO_2 and 8% Eu/ CeO_2 samples. The diffraction features centered at about 28.5° , 33.1° , 47.4° , 56.3° and 59.0° correspond to the (111), (200), (220), (311) and

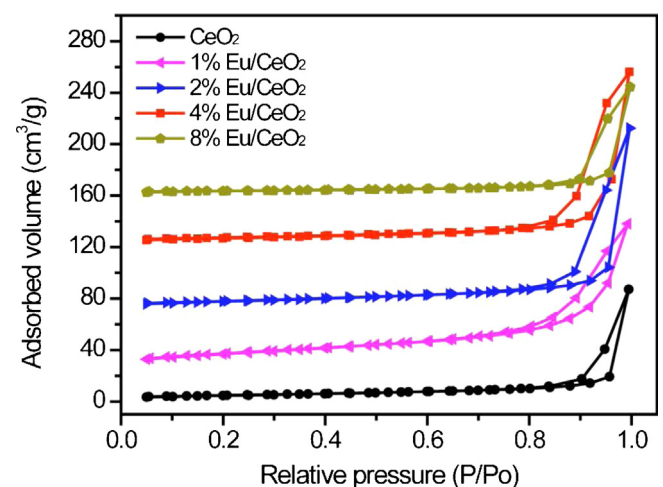


Fig. 3. Nitrogen adsorption–desorption isotherm of CeO_2 nanosheets, 1% Eu/ CeO_2 nanosheets, 2% Eu/ CeO_2 nanosheets, 4% Eu/ CeO_2 nanosheets, and 8% Eu/ CeO_2 nanosheets.

(222) planes of the cubic phase of CeO_2 (PDF#34-0394). It should be mentioned that only the diffraction peaks of the CeO_2 phase can be observed, and no diffraction peaks of Eu_2O_3 , indicating that there

Table 1Specific surface areas and Eu contents of Eu/CeO₂ catalysts.

Sample	The content of Eu%	BET surface area m ² /g	Pore volume cm ³ /g	Pore size Å
CeO ₂	0	12.53	0.13	418.37
1% Eu/Ce ₂	0.99	16.87	0.14	320.17
2% Eu/Ce ₂	1.97	25.34	0.21	332.82
4% Eu/Ce ₂	3.97	28.24	0.22	312.48
8% Eu/Ce ₂	7.98	20.35	0.19	312.48

was no obvious change in the lattice parameters after the Eu was introduced. Significantly, the (1 1 1) reflection shifts toward higher 2θ value with increasing concentration of Eu, which may be due to an increase in oxygen vacancies concentration [25]. This further confirms that the Eu ions are incorporated into the CeO₂ lattice.

3.3. Morphology

The morphologies of Eu-doped CeO₂ nanosheets were determined by scanning electron microscopy (SEM). As shown in Fig. 2a–f, the as-formed nanosheets of the 4% Eu/CeO₂ with a lateral size of several hundred nanometers are intercrossed with one another. The thickness of the nanosheet is around 50 nm, which creates loose porous nanostructures with abundant open space and surface sites. It can be observed that there were no differences in the nanosheet of the other samples after the Eu doping. The detail morphology of 4% Eu/CeO₂ nanosheets was further examined by transmission electron microscopy (TEM). Fig. 2g displays a typical TEM image of 4% Eu/CeO₂ nanosheets, from which the 4% Eu/CeO₂ nanosheets can be clearly identified. Selected-area electron diffrac-

tion (SAED) analyses reveal that the 4% Eu/CeO₂ nanosheets is poly-crystalline structure. Fig. 2h displays a typical high-resolution TEM (HRTEM) image of the 4% Eu/CeO₂ nanosheets. Well-resolved lattice fringes of 0.27 nm corresponding to the (2 0 0) interplanar spacing of cubic phase of CeO₂, was clearly observed.

3.4. Specific surface area measurements

The porous structure and texture of the samples were investigated by N₂ sorption analysis. Fig. 3 demonstrated the nitrogen adsorption–desorption isotherms for CeO₂, 1% Eu/CeO₂, 2% Eu/CeO₂, 4% Eu/CeO₂, 8% Eu/CeO₂ samples. The isotherms of all the samples are similar to each other and can be classified as type IV, possessing a distinct H₃-type hysteresis loop at a relative pressure ranges of 0.69–1.0 P/P₀ [26], which indicates the typical mesoporous characteristics of the entire samples. The pore structure parameters for all the samples including BET specific surface area (S_{BET}), pore volume (V_p) and pore width (d_p) are listed in Table 1. The 4% Eu/CeO₂ (28.24 m²/g) sample exhibited specific surface area of 28.24 m²/g and the pore volume of 0.22 cm³/g, which

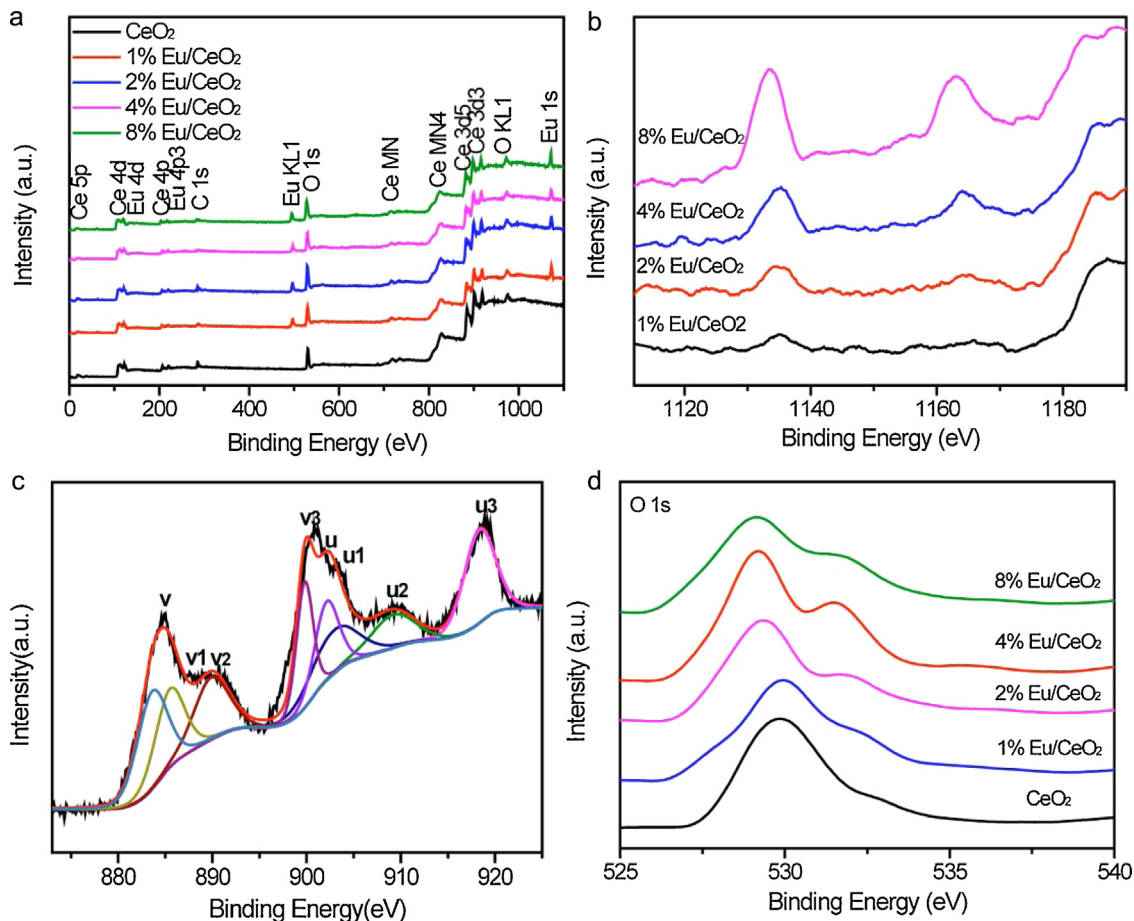


Fig. 4. (a) XPS survey patterns, (b) Core level Eu 1s XPS spectra, (c) Core level Ce 3d XPS spectra of 4% Eu/CeO₂ nanosheets, (d) Core level O 1s XPS spectra of CeO₂ nanosheets, 1% Eu/CeO₂ nanosheets, 2% Eu/CeO₂ nanosheets, 4% Eu/CeO₂ nanosheets, 8% Eu/CeO₂ nanosheets.

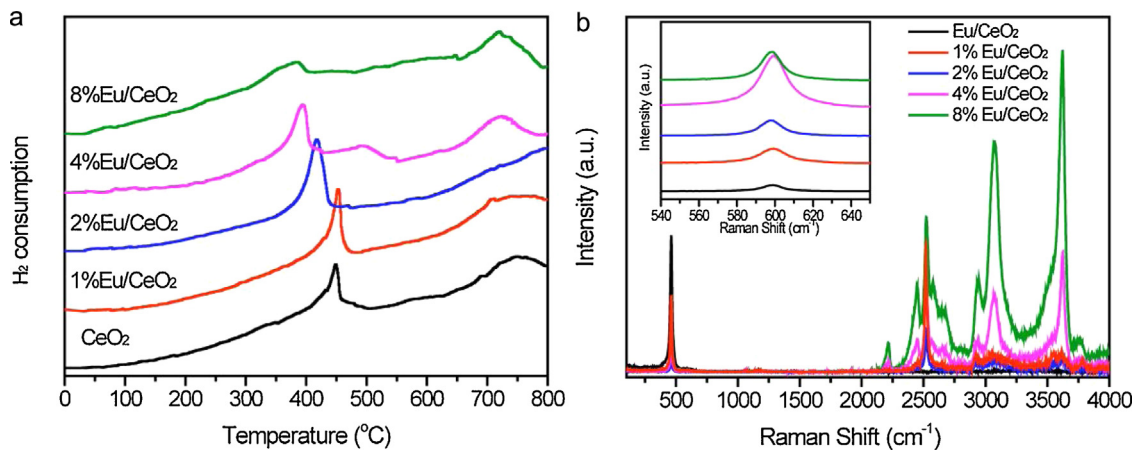


Fig. 5. (a) H₂-TPR profiles, (b) Raman patterns of CeO₂ nanosheets, 1% Eu/CeO₂ nanosheets, 2% Eu/CeO₂ nanosheets, 4% Eu/CeO₂ nanosheets, 8% Eu/CeO₂ nanosheets.

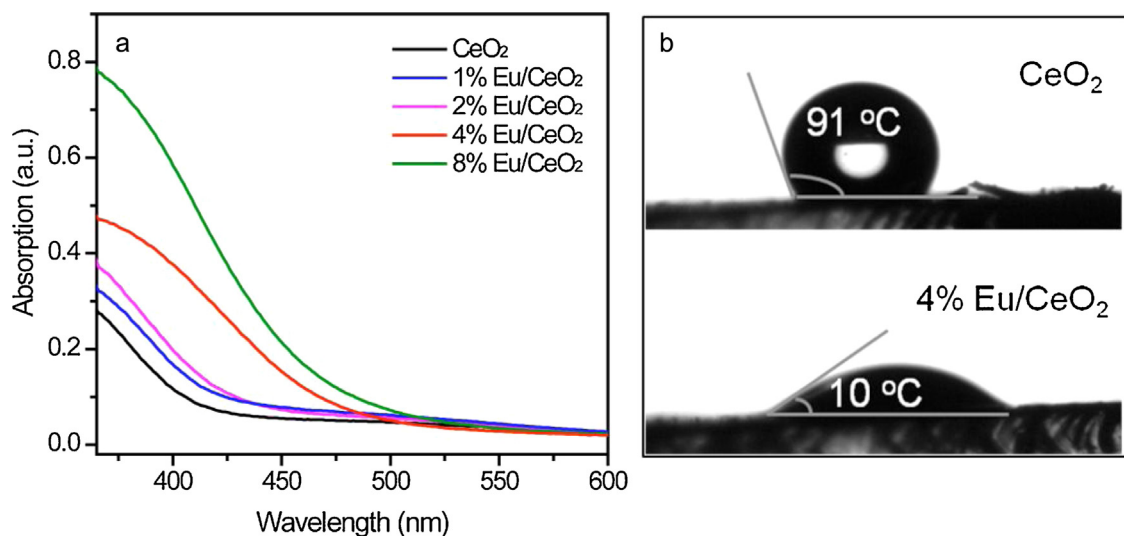


Fig. 6. (a) UV-vis absorption spectra of all the CeO₂ catalysts. (b) Contact angles of a HCHO droplet on CeO₂ nanosheets and 4% Eu/CeO₂ nanosheets.

is larger than the values obtained for 8% Eu/Ce₂ (20.35 m²/g and 0.19 cm³/g); and CeO₂ showed the lowest *S_{BET}* and *V_p* (12.53 m²/g and 0.13 cm³/g). In general, the larger specific surface area and pore volume of the 4% Eu/CeO₂ sample can provide more absorption and/or reacting sites for HCHO, which results in higher catalytic activity.

3.5. XPS studies

The X-ray photoelectron spectroscopy (XPS) was carried out to study the compositions and redox behavior of all CeO₂-based samples. Fig. 4 presents the Eu 1s, Ce 3d and O 1s XPS spectra of CeO₂, 1% Eu/CeO₂, 2% Eu/CeO₂, 4% Eu/CeO₂, 8% Eu/CeO₂ samples. It can be seen from Fig. 4a that the samples consist of Ce, Eu, and O elements. The carbon peak is attributed to adventitious from the XPS instrument. The XPS results of Eu 1s signals were detected in the Eu-doped CeO₂ nanosheets confirming the presence of Eu in the CeO₂. It is worthy to point that the intensity of the Eu signal increases with increasing content of Eu. The Ce 3d XPS spectra were analyzed in order to ascertain the oxidation state of cerium. Eight peaks can be found in Ce 3d XPS spectra of all the tested samples, which are labeled as u, u₁, u₂, u₃, v, v₁, v₂ and v₃, respectively (Fig. 4c and Fig. S1). The peaks labeled as u, u₂ and u₃ refer to Ce⁴⁺ 3d_{3/2}, and the peaks labeled as v, v₂ and v₃ refer to Ce⁴⁺ 3d_{5/2}. The characteristic peaks of Ce³⁺ 3d_{3/2} and 3d_{5/2} states are labeled as u₁ and v₁,

respectively. The presence of Ce³⁺ is due to the reduction of Ce⁴⁺ in the oxide structure. The calculated ratio of Ce³⁺ for the CeO₂, 1% Eu/CeO₂, 2% Eu/CeO₂, 4% Eu/CeO₂ and 8% Eu/CeO₂ are 13.47, 14.21, 14.89, 18.54 and 18.52%, respectively. The 4% Eu/CeO₂ catalyst composed of abundant Ce³⁺ ions, which provide sufficient active sites for the oxidation reaction and hence, enhanced its catalytic ability. Moreover, the XPS results of O1s signals were carried out to interpret the chemical states of oxygen on the surface of CeO₂-based samples. As showed in Fig. 4d, there are two major peaks, namely the lattice oxygen and surface active oxygen. After doping Eu, more oxygen vacancies are easily formed in the CeO₂. This seems to favor the catalytic activity because they could provide sites for oxygen activation to form superoxide (O²⁻) species, which was considered as the intermediate species in the reactions occurring on the catalysts surface. Hence, the 4% Eu/CeO₂ nanosheets have the highest defective oxygen concentration, which could account for its superior catalytic performance over the other catalysts.

3.6. Temperature-programmed reduction (TPR) measurements and Raman spectroscopy

A large amount of information on the redox behavior of CeO₂ has been obtained by temperature-programmed reduction (TPR) measurements, which can provide insights into low- and high-temperature interactions between H₂, and CeO₂. As displayed in

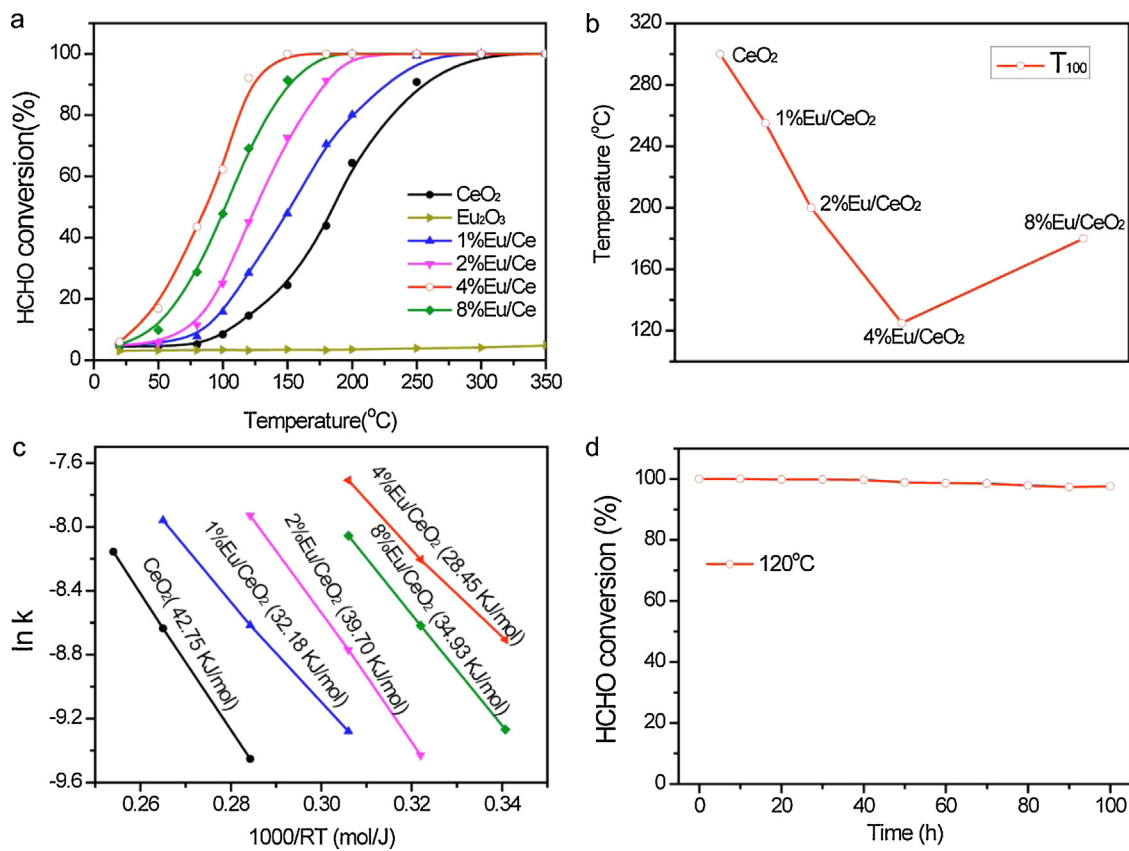


Fig. 7. (a) HCHO catalytic performance of the different catalysts under the following conditions: HCHO concentration = 50 ppm, 25 vol% O_2 , N_2 as balance gas, $\text{GSHV} = 30,000 \text{ mL h}^{-1} \text{ g}^{-1}$. (b) The temperature of all the catalysts completely conversion HCHO. (c) Arrhenius plots for oxidation of HCHO on the all catalysts. (d) HCHO catalytic performance with time on stream over the 4% Eu/CeO_2 catalysts at 120 °C.

Fig. 5a, CeO_2 shows two reduction peaks at 420–789 °C. The peak at low temperature (420 °C) is attributed to reduction of surface active oxygen, while the peak at high temperature (789 °C) indicate the reduction of the lattice oxygen [27]. After doping of Eu^{3+} into CeO_2 , the peak of the surface active oxygen moved to the low temperature region. Noticeably, a new peak appear at 495 °C, which may be related to the more surface active oxygen in 4% Eu/CeO_2 nanosheets catalyst. All these results reveal that Eu-doped CeO_2 nanosheets possess high redox ability. Furthermore, **Fig. 5b** shows the Raman spectroscopy of the CeO_2 , 1% Eu/CeO_2 , 2% Eu/CeO_2 , 4% Eu/CeO_2 and 8% Eu/CeO_2 samples, further revealing the presence of oxygen vacancies in the structure of the Eu-doped CeO_2 . The band at 465 cm^{-1} is attributed to Raman active vibrational mode of fluorite-type CeO_2 , while that at 600 cm^{-1} is related to oxygen vacancies due to the presence of Ce^{3+} and Eu^{3+} in the CeO_2 lattice. Another peak appears after 2000 cm^{-1} with the introduction of Eu into the lattice, and the band intensity increases as the amount of Eu increases. Combining with the Raman and XPS characterizations above, we can conclude that oxygen vacancies are successfully introduced to the CeO_2 nanosheets.

3.7. UV-vis diffuse reflectance spectra and Contact angle

Fig. 6a shows UV-vis absorption spectra of CeO_2 , 1% Eu/CeO_2 , 2% Eu/CeO_2 , 4% Eu/CeO_2 and 8% Eu/CeO_2 samples. Only an absorption band, which is attributed to the band-to-band transition, can be observed in the UV region for CeO_2 nanosheets. The absorption band edge of the Eu-doped CeO_2 nanosheets exhibited red shift compared to the CeO_2 nanosheets. It was observed that the absorption was gradually enhanced with increase in the content

of Eu. As for the 8% Eu/CeO_2 sample, it exhibits a wide and strong absorption range of 350–510 nm, which suggests that it can use the solar light. This may be due to the introduction of oxygen vacancies in the CeO_2 that can intrinsically improve the optical absorption property of CeO_2 . This result also reveals the successful fabrication of oxygen vacancies into the CeO_2 nanosheets. As an indirect semiconductor, the band gap of Eu-doped CeO_2 nanosheets can be calculated from the plot of $(\alpha h\nu)^{1/2}$ versus photon energy ($h\nu$) (Supporting Information Fig. S2), which is 2.23 eV for the 4% Eu/CeO_2 nanosheets and much smaller than those of 1% Eu/CeO_2 (2.50 eV), 2% Eu/CeO_2 (2.4 eV), and CeO_2 (2.55 eV) counterparts. This convincingly supports that oxygen vacancies could narrow the band gap and enhance the optical absorption, which believed to be another major reason for the superior photocatalytic activity of 4% Eu/CeO_2 nanosheets. Additionally, contact angle test was carried out in order to investigate the surface contact of HCHO and catalysts. Contact angle can be defined as the angle between the solid surface and liquid–air interface, measured through the liquid phase, which show the wettability of a solid surface and used to determine the adhesion force between a drop and solid surface. **Figs. 6b** and S3 show the contact angle photographs between the HCHO and catalysts under the room temperature. Interestingly, the contact angle decreases from 105° to 10° after the Eu was doped into the CeO_2 nanosheets, which indicates the adhesion force is significantly enhanced. Such characters for accommodation of the HCHO may speed up the HCHO penetration and spreading in the channels of Eu-doped CeO_2 catalysts, which may increase the contact area with HCHO and subsequently, improving the active material utilization.

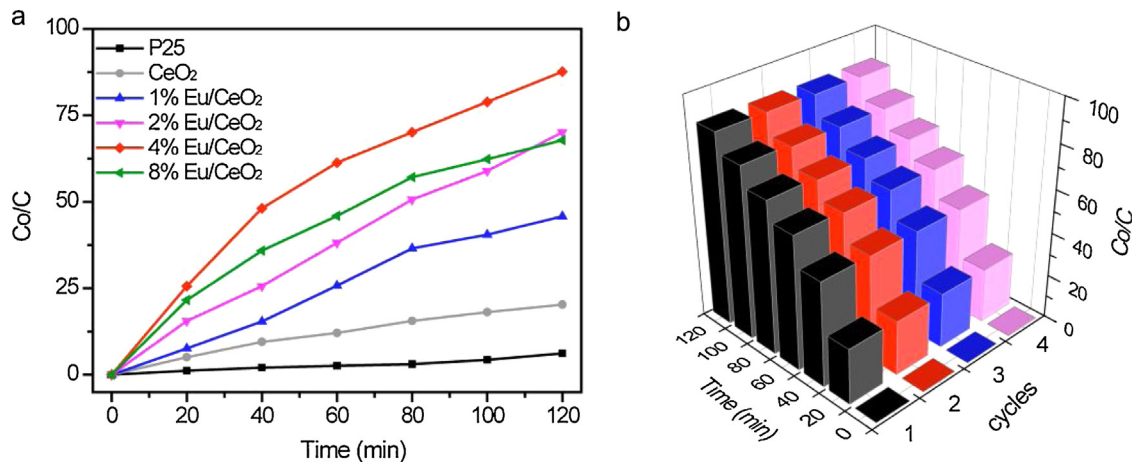


Fig. 8. (a) Photocatalytic activity of the catalysts for degradation of HCHO gas under visible light irradiation. (b) Photocatalytic activity of the 4% Eu/CeO₂ nanosheets for degradation of HCHO gas with 4 cycles visible light irradiation.

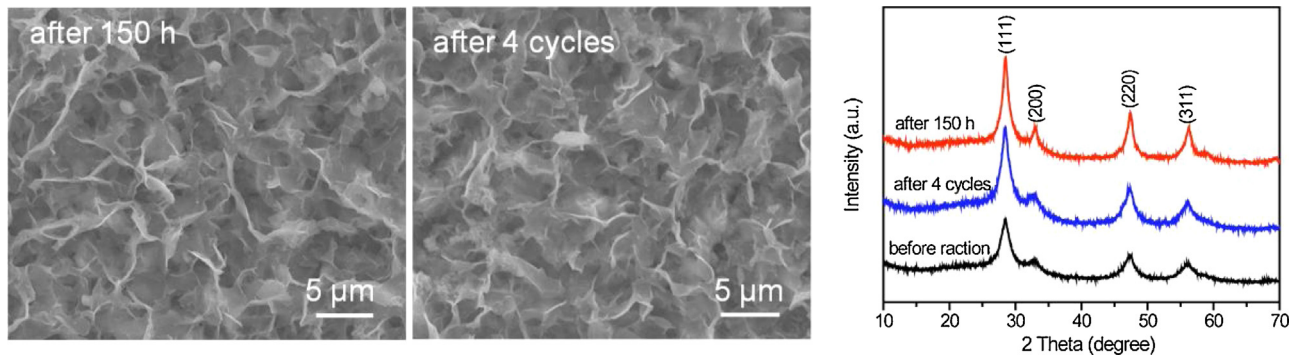


Fig. 9. SEM pictures and XRD pattern of 4% Eu/CeO₂ nanosheets after reaction for 150 h and after 4 cycles.

3.8. Thermal catalytic activity of all CeO₂-based nanosheets

Recently, CeO₂ have been tested for oxidation of HCHO due to its thermal and redox ability. Its operating temperature is in the range of 200–300 °C, and their catalytic efficiency is inadequate for technological adaptation. Noble metal catalysts such as Pt [6] and Au [28,29] could effectively convert HCHO into CO₂ and H₂O at low temperature. The oxygen mobility in CeO₂ support is important for the catalysts, since the oxygen from the support is available for HCHO oxidation. However, the high cost of noble metals hinders their practical application. Therefore, it is still a challenge to improve the performance of CeO₂ for HCHO oxidation at low temperature without the noble metals.

The Eu-doped CeO₂ nanosheets are first evaluated for HCHO oxidation. Fig. 7a shows the catalytic activity of different catalysts with increasing reaction temperature. For comparison, pure Eu₂O₃ are also characterized for the HCHO oxidation, which did not show obvious catalytic activity. Generally, the doping of Eu significantly enhanced catalytic performance of CeO₂. The complete HCHO oxidation of 4% Eu/CeO₂ nanosheets can be obtained at 120 °C, which is 200 °C lower than that of the pure CeO₂ (310 °C) and lower than that of 1% Eu/CeO₂ (290 °C), 2% Eu/CeO₂ (225 °C), and 8% Eu/CeO₂ (180 °C) as shown in Fig. 7b. Besides, the effect of GHSV on the catalytic property of 4% Eu/CeO₂ nanosheets was also investigated (Fig. S4). It is found that at the space velocity of GHSV of 15,000 mL h⁻¹ g⁻¹, the complete-conversion temperature was 115 °C, which is significantly lower than those space velocities at 30,000 mL h⁻¹ g⁻¹ (120 °C), 60,000 mL h⁻¹ g⁻¹ (150 °C), 120,000 mL h⁻¹ g⁻¹ (196 °C). This present complete-conversion temperature of the 4% Eu/CeO₂

nanosheets is also considerably lower than the values recently reported for MnO_x–CeO₂ ($T_{100} = 150$ °C, 30,000 mL h⁻¹ g⁻¹) [30], 3D-Co₃O₄ ($T_{100} = 130$ °C, 30,000 mL h⁻¹ g⁻¹) [31], mesoporous MnO_x ($T_{100} = 160$ °C, 30,000 mL h⁻¹ g⁻¹) [32], MnO_x–SnO₂ ($T_{100} = 180$ °C, 30,000 mL h⁻¹ g⁻¹) [33], MnO₂/cellulose ($T = 150$ °C, 50,000 mL h⁻¹ g⁻¹) [34], and slightly higher than the hollow K_xMnO₂ nanospheres ($T_{100} = 140$ °C, 50,000 mL h⁻¹ g⁻¹) [35], 0.34%Au/CeO₂ ($T_{100} = 140$ °C, 34,000 mL h⁻¹ g⁻¹) [36], 3D-Mn_{0.5}Co_{2.25}O₄ ($T_{100} = 75$ °C, 120,000 mL h⁻¹ g⁻¹) [37], 2.5%Au/CeO₂ ($T_{100} = 75$ °C, 50,000 mL h⁻¹ g⁻¹) [28]. Meanwhile, Arrhenius plots for the catalysts of HCHO oxidation were showed in Fig. 7c. The 4% Eu/CeO₂ catalyst has the lowest activation energy (28.45 kJ/mol), which is much lower than the CeO₂ catalyst (42.75 kJ/mol), 1% Eu/CeO₂ (32.18 kJ/mol), 2% Eu/CeO₂ (39.70 kJ/mol), 8% Eu/CeO₂ (34.93 kJ/mol). The low activation energy means that HCHO reaction was much easier on the catalyst surface. It is clear that Eu doped CeO₂ could efficiently improve the HCHO oxidation. This is because the doped Eu ions could promote the formation of oxygen vacancy, enhanced the redox ability, and then allows easier surface reaction, which is in favour of HCHO oxidation. All the results above show that 4% Eu/CeO₂ catalyst have the superior activity for HCHO oxidation. Additionally, the initial CO₂ selectivity is only 0.2%, indicating that not all the removed HCHO was oxidized and some of them were adsorbed on the surface of 4% Eu/CeO₂ catalysts (Fig. S5). The CO₂ selectivity was gradually increased along with the temperature and reached a stable value as high as 99%, demonstrating that most of the removed HCHO was oxidized into CO₂. Some CO was generated from incomplete oxidation of HCHO.

To estimate the stability of the catalyst, we carried out a long time HCHO reaction. The 4% Eu/CeO₂ catalyst was used for the sta-

bility test due its excellent performance in the above result. The HCHO oxidation over 4% Eu/CeO₂ was carried out at 120 °C for 100 h. As displayed in Fig. 7d, the 4% Eu/CeO₂ shows an excellently catalytic stability without any loss of its HCHO conversion as long as 100 h. With this result, it is apparent that the catalyst exhibit high performance with good stability.

3.9. Photocatalytic performance of all the CeO₂-based nanosheets

Photocatalysis has been received as a great promising method toward solving environment problems with abundant solar light [11,38,39]. In the past few years, many works have demonstrated the introduction of oxygen vacancies or increasing the density of oxygen vacancies at the surface of the photocatalyst can inhibit the recombination of electron-hole pairs while improving the photocatalysis [40]. Likewise, doping has been regarded as an important way to introduce oxygen vacancies and then enhanced photocatalytic activity [41,42]. For example, Liyanage et al. reported that doping Y into CeO₂ nanorods can improve the photocatalytic performance of organic dyes degradation [43]. Nitrogen-doped TiO₂ has an improvement over TiO₂ under visible light in optical absorption and photocatalytic activity such as photodegradations of methylene blue and gaseous acetaldehyde [44]. Therefore, we proposed that our as-prepared Eu-doped CeO₂ nanosheets could be an efficient catalyst for photocatalytic oxidation of gaseous HCHO.

The Eu/CeO₂ samples are thus evaluated as photocatalysts for removing gaseous HCHO (500 ppm), and the photocatalytic property of P25 was also evaluated as a comparison. Fig. 8a shows the course of HCHO purification for the CeO₂, 1% Eu/CeO₂, 2% Eu/CeO₂, 4% Eu/CeO₂, 8% Eu/CeO₂, and P25 under visible light ($\lambda > 420$ nm). In the present system, the degradation of HCHO by the P25 was almost negligible after 120 min under the visible light irradiation. Eu/CeO₂ samples exhibit higher photocatalytic activity compared to pure CeO₂ and P25. As shown in Fig. 6a, the 4% Eu/CeO₂ catalysts has the highest photocatalytic activity and achieved 80% higher degradation compared to pure CeO₂ and P25. However, the photocatalytic efficiency decreases with increasing amount of oxygen vacancies, which indicate that much oxygen vacancies show a decreased photocatalytic activity. The improvement could be attributed to the following reasons; First, the 4% Eu/CeO₂ catalyst have a larger surface area, which could absorb more HCHO in the surface and more active sites for HCHO reaction. Second, the 4% Eu/CeO₂ demonstrate enhanced optical absorption in the visible region, indicating that the 4% Eu/CeO₂ nanosheets could utilize more solar light. Third, suggested by previous work, the oxygen vacancies could effectively separates the photo-induced electron-hole pairs. However, the separation of electron-hole pairs is related to the amount of oxygen vacancies present, thus, much more oxygen vacancies would allow fast electron-hole recombination, thereby decreasing the photocatalytic activity. Therefore, we conclude that the distinction in photocatalytic performance is mainly sourced from the different amount of oxygen vacancies. In order to study the reaction mechanism, we performed the photocatalytic reaction without O₂. The 4% Eu/CeO₂ sample exhibited substantially higher efficiency photocatalytic performance with the addition of O₂ than that of without the addition of O₂ (Fig. S6a), which shows that the presence of O₂ can further improve the photocatalytic activity of the 4% Eu/CeO₂. Thus, the reaction mechanism was shown in the Fig. S6b. Under the irradiation, the photo-generated holes of the CeO₂ can transfer to the Eu₂O₃, resulting in the efficient separation of photo-generated electron-hole pairs. Then, the holes react with the HCHO and produce the CO₂ and H₂O. The electron can react with oxygen molecules to finally form active oxygen, which can also react with the HCHO. Hence, the enhanced charge transportation and improved light-harvesting ability induced by oxygen vacancies are

believed to be the major reasons for the superior photocatalytic activity of 4% Eu/CeO₂ catalysts. In the photocatalytic oxidation of HCHO, no other carbon containing compounds except CO₂ in the products were detected. The produce CO₂ selectivity is almost 100%, indicating that all the removed HCHO was completely oxidized into CO₂ and H₂O.

To study the thermal effect in the photocatalytic reaction, we performed the photocatalytic reaction at high temperature. Fig. S7 shows the photocatalytic performance of 4% Eu/CeO₂ nanosheets catalysts at different temperature. The samples exhibited higher activity when the temperature increased. Note that the activity at 25 °C was almost the same as this at 50 °C, which revealed that the thermal effect under 50 °C can be ignored in photo-catalytic reaction.

In order to investigate the stability of the as-prepared 4% Eu/CeO₂ nanosheets, recycling tests of the visible-driven photodegradation activity of HCHO were performed for certain times on the recycled 4% Eu/CeO₂ sample. As shown in Fig. 8b, it is interesting to note that after 4 cycles, nearly 97% of the photocatalytic efficient is retained for the 4% Eu/CeO₂ sample, apparently justifying that the 4% Eu/CeO₂ has the best cycling stability among the tested samples at the same testing condition.

Fig. 9 shows the SEM images of the 4% Eu/CeO₂ sample after 100 h long HCHO reaction and after 4 cycles photocatalytic reaction. It revealed that there is no morphological change after 100 h long HCHO reaction and after 4 cycles photocatalytic reaction. Also, XRD of the 4% Eu/CeO₂ catalyst after HCHO reaction for 100 h and after 4 cycles photocatalytic reaction were the same with the catalyst before reaction. Thus, these results fully confirm that the Eu-doped CeO₂ have the good thermal stability and photocatalytic stability for HCHO oxidation.

4. Conclusions

In summary, Eu-doped CeO₂ nanosheets with different amounts of Eu were synthesized by electrodeposition. The composition of the Eu-doped CeO₂ nanosheets can be easily tuned by adjusting the ratio of Eu to Ce. Significantly, the doping of Eu cations promoted the formation of oxygen vacancies, enhanced the redox ability, enhanced optical absorption and allows much easier surface reaction. The as-prepared Eu/CeO₂ catalyst is evaluated as a material for catalytic oxidation of formaldehyde and also as a visible light photocatalyst for HCHO degradation. Remarkably, the 4% Eu/CeO₂ catalyst did not only exhibits high performance of complete oxidation HCHO at the low temperature of 120 °C, but also significantly enhanced photocatalytic activity for HCHO gas degradation under visible light irradiation. Additionally, it shows higher stability for oxidation HCHO and photocatalysis. These results demonstrate the promising use of properly designed multifunction materials in energy storage, photocatalysis, and other areas.

Acknowledgments

This work was preliminarily supported by supported by the Natural Science Foundation of China (21425627 and 21476271), the Science and Technology Plan Project (2013B090600036) and Natural Science Foundation (2014A030308012 and 2014KTSCX004) of Guangdong Province, China.

Appendix A. Supplementary data

Supplementary data associated with this article can be found, in the online version, at <http://dx.doi.org/10.1016/j.apcatb.2015.08.047>.

References

[1] J. Yu, X. Li, Z. Xu, W. Xiao, *Environ. Sci. Technol.* 47 (2013) 9928–9933.

[2] P. Zhou, X. Zhu, J. Yu, W. Xiao, *ACS Appl. Mater. Interfaces* 5 (2013) 8165–8172.

[3] W.J. Liang, J. Li, J.X. Li, T. Zhu, Y.Q. Jin, *J. Hazard. Mater.* 175 (2010) 1090–1095.

[4] P. Fu, P. Zhang, J. Li, *Appl. Catal. B: Environ.* 105 (2011) 220–228.

[5] X. Chen, H.Y. Zhu, J.C. Zhao, Z.F. Zheng, X.P. Gao, *Angew. Chem. Int. Ed.* 120 (2008) 5433–5436.

[6] C. Zhang, F. Liu, Y. Zhai, H. Ariga, N. Yi, Y. Liu, K. Asakura, H. M. Flytzani-Stephanopoulos, *Angew. Chem. Int. Ed.* 51 (2012) 9628–9632.

[7] G. Vilé, F. Colussi, A. Krumeich, J. Trovarelli, A. Troparelli, *Angew. Chem. Int. Ed.* 126 (2014) 12265–12268.

[8] Q. Xu, W. Lei, X. Li, X. Qi, J. Yu, G. Liu, J. Wang, P. Zhang, *Environ. Sci. Technol.* 48 (2014) 9702–9708.

[9] A. Corma, P. Atienzar, H. Garcia, J.Y. Chane-Ching, *Nat. Mater.* 3 (2004) 394–397.

[10] K.H. Ye, S.A. Zhou, X.C. Zhu, C.W. Xu, P.K. Shen, *Electrochim. Acta* 90 (2013) 108–111.

[11] W. Lei, T. Zhang, L. Gu, P. Liu, J.A. Rodriguez, G. Liu, M. Liu, *ACS Catal.* (2015), <http://dx.doi.org/10.1021/acscatal.5b00560>.

[12] V. Shapovalov, H. Metiu, *J. Catal.* 245 (2007) 205–214.

[13] Z.Y. Pu, X.S. Liu, A.P. Jia, Y.L. Xie, J.Q. Lu, M.F. Luo, *J. Phys. Chem. C* 112 (2008) 15045–15051.

[14] Q. Xie, Y. Zhao, H. Guo, A. Lu, X. Zhang, L. Wang, M.S. Chen, D.L. Peng, *ACS Appl. Mater. Interfaces* 6 (2013) 421–428.

[15] J. Kwon, A.A. Sharma, J.A. Bain, Y.N. Picard, M. Skowronski, *Adv. Funct. Mater.* 25 (2015) 2876–2883.

[16] Y. Lv, Y. Liu, Y. Zhu, Y. Zhu, *J. Mater. Chem. A* 2 (2014) 1174–1182.

[17] T. Sayle, S. Parker, C. Catlow, *Surf. Sci.* 316 (1994) 329–336.

[18] P. Vidmar, P. Fornasiero, J. Kašpar, G. Gubitoso, M. Graziani, *J. Catal.* 171 (1997) 160–168.

[19] E. Mamontov, T. Egami, R. Brezny, M. Koranne, S. Tyagi, *J. Phys. Chem. B* 104 (2000) 11110–11116.

[20] C.E. Hori, H. Permana, K.S. Ng, A. Brenner, K. More, K.M. Rahmoeller, D. Belton, *Appl. Catal. B: Environ.* 16 (1998) 105–117.

[21] F. Wang, Y. Han, C.S. Lim, Y. Lu, J. Wang, J. Xu, H. Chen, C. Zhang, M. Hong, X. Liu, *Nature* 463 (2010) 1061–1065.

[22] G.R. Li, D.L. Qu, L. Arurault, Y.X. Tong, *J. Phys. Chem. C* 113 (2009) 1235–1241.

[23] L. Li, H.K. Yang, B.K. Moon, Z. Fu, C. Guo, J.H. Jeong, S.S. Yi, K. Jang, H.S. Lee, *J. Phys. Chem. C* 113 (2008) 610–617.

[24] H. Guo, Y. Qiao, *Appl. Surf. Sci.* 254 (2008) 1961–1965.

[25] S.B. Bošković, D.R. Djurović, S.P. Zec, B.Z. Matović, M. Zinkevich, F. Aldinger, *Ceram. Int.* 34 (2008) 2001–2006.

[26] L. Zhang, L. Shi, L. Huang, J. Zhang, R. Gao, D. Zhang, *ACS Catal.* 4 (2014) 1753–1763.

[27] L. Ma, D. Wang, J. Li, B. Bai, L. Fu, Y. Li, *Appl. Catal. B: Environ.* 148 (2014) 36–43.

[28] H.F. Li, N. Zhang, P. Chen, M.F. Luo, J.Q. Lu, *Appl. Catal. B: Environ.* 110 (2011) 279–285.

[29] B. Liu, Y. Liu, C. Li, W. Hu, P. Jing, Q. Wang, J. Zhang, *Appl. Catal. B: Environ.* 127 (2012) 47–58.

[30] X. Tang, Y. Li, X. Huang, Y. Xu, H. Zhu, J. Wang, W. Shen, *Appl. Catal. B: Environ.* 62 (2006) 265–273.

[31] B. Bai, H. Arandian, J. Li, *Appl. Catal. B: Environ.* 142 (2013) 677–683.

[32] J.Q. Torres, J.M. Giraudon, J.F. Lamonier, *Catal. Today* 176 (2011) 277–280.

[33] Y. Wen, X. Tang, J. Li, J. Hao, L. Wei, X. Tang, *Catal. Commun.* 10 (2009) 1157–1160.

[34] L. Zhou, J. He, J. Zhang, Z. He, Y. Hu, C. Zhang, H. He, *J. Phys. Chem. C* 115 (2011) 16873–16878.

[35] H. Chen, J. He, C. Zhang, H. He, *J. Phys. Chem. C* 111 (2007) 18033–18038.

[36] Y. Shen, X. Yang, Y. Wang, Y. Zhang, H. Zhu, L. Gao, M. Jia, *Appl. Catal. B: Environ.* 79 (2008) 142–148.

[37] Y. Wang, X. Zhu, M. Crocker, B. Chen, C. Shi, *Appl. Catal. B: Environ.* 160 (2014) 542–551.

[38] H. Li, Y. Zhou, W. Tu, J. Ye, Z. Zou, *Adv. Funct. Mater.* (2015).

[39] K.J. Ju, M. Zhang, Q.L. Zhang, J. Wei, A.J. Wang, *Nature* 16 (2015) 17.

[40] Y. Huang, H. Li, M.S. Balogun, W. Liu, Y. Tong, X. Lu, H. Ji, *ACS Appl. Mater. Interfaces* 6 (2014) 22920–22927.

[41] T. Ihara, M. Miyoshi, Y. Iriyama, O. Matsumoto, S. Sugihara, *Appl. Catal. B: Environ.* 42 (2003) 403–409.

[42] M.V. Sofianou, M. Tassi, V. Psycharis, N. Boukos, S. Thanos, T. Vaimakis, J. Yu, C. Trapalis, *Appl. Catal. B: Environ.* 162 (2015) 27–33.

[43] A.D. Liyanage, S.D. Perera, K. Tan, Y. Chabal, K.J. Balkus Jr., *ACS Catal.* 4 (2014) 577–584.

[44] R. Asahi, T. Morikawa, T. Ohwaki, K. Aoki, Y. Taga, *Science* 293 (2001) 269–271.